

Relativistic Tidal Dissipation and the Gravitational-wave Signal of a White Dwarf Orbiting an Intermediate-Mass Black Hole

Yang Yang,^{1,2} Leif Lui,³ Alejandro Torres-Orjuela,³ and Xian Chen^{1,2,*}

¹*Department of Astronomy, School of Physics, Peking University, 100871 Beijing, China*

²*Kavli Institute for Astronomy and Astrophysics, Peking University, 100871 Beijing, China*

³*Beijing Institute of Mathematical Sciences and Applications, Beijing 101408, China*

(Dated: February 27, 2026)

Finding intermediate-mass black holes (IMBHs) and measuring their masses and spins are key to understanding massive black hole formation. White dwarf (WD)–IMBH binaries provide a unique probe because they emit both electromagnetic radiation and gravitational waves (GWs), thereby conveying richer information. However, such multi-messenger sources often enter the regime of strong gravity, where existing models often fail to capture their relativistic dynamics. Here, we develop a fully relativistic model for the tidal response of a WD close to an IMBH, and use it to study the secular orbital evolution as well as the GW signal. We find that for IMBHs more massive than $10^5 M_\odot$, tidal interaction becomes relativistic and sensitive to IMBH spin. The interaction generally dissipates binary orbital energy and angular momentum, but due to relativistic frame rotation, which reduces phase coherence across pericenter passages, the orbit-averaged tidal dissipation rate can be suppressed by up to $\sim 50\%$ relative to Newtonian predictions. Including tidal dissipation leads to more rapid damping of the orbital eccentricity, to the extent that the pericenter distance may even increase over time, potentially explaining quasi-periodic eruptions and secular orbital period growth. Such tidal effect accumulates into measurable phase and amplitude deviations in the GW signal. For typical space-based observations, the GW waveform mismatch can reach $\mathcal{O}(0.1)$ within 6 months. Our results indicate that relativistic tidal dissipation is both dynamically important and observationally essential for reliably predicting the multi-messenger signals of WD-IMBH systems.

I. INTRODUCTION

Intermediate-mass black holes (IMBHs), with masses in the range of $M_\bullet \sim 10^2 - 10^5 M_\odot$, fill the intriguing gap between stellar-mass black holes (BHs) and supermassive BHs. Their mass and spin in principle encode unique information about how the most massive BHs in the universe come into being [1–3]. Their spatial and redshift distributions are also expected to hold vital clues about the role massive BHs play in shaping their host galaxies [4–6]. However, despite many efforts to find their electromagnetic (EM) signatures using conventional astronomical methods, observational evidence for IMBHs remains scarce [6–8].

The detection of gravitational waves (GWs) in the past decade by ground-based interferometers [9, 10] and pulsar timing arrays [11–15] opens up new possibilities of finding IMBHs. It has been predicted that in dense stellar environments such as globular clusters, IMBHs can capture compact objects, such as stellar-mass BHs or other IMBHs, and a fraction of such binaries can coalesce via GW radiation within a Hubble time [16–20]. During the last few months of evolution, these binaries emit GWs in the frequency band of $10^{-3} - 0.1$ Hz, which is the optimal observational band for space GW missions such as LISA, Taiji, TianQin, and lunar-based detectors [21–24].

Among the systems that may harbor IMBHs, a binary composed of an IMBH and a white dwarf (WD)

stands out as a unique multi-messenger target because it emits both EM and GW signals during its last evolutionary stage [25–28]. On one hand, before the WD falls beyond the event horizon of the IMBH, mass transfer (MT) or tidal disruption can happen [29–32]. They produce EM counterparts. On the other hand, thanks to the relatively high density of WD, tidal disruption events (TDEs) or MT occur not too far from the event horizon of the IMBH, creating a strong-field dynamical condition for powerful GW emission [27, 28, 33]. Therefore, a joint detection of EM and GW signals would unambiguously place the (otherwise hidden) BH in the intermediate-mass range and significantly improve parameter estimation by breaking degeneracies inherent to GW-only observations [32, 34–36].

We may have already witnessed the EM outbursts of these relativistic WD-IMBH binaries. It has been suggested that the population of X-ray transients known as quasi-periodic eruptions (QPEs) are possibly such mass-transferring systems whose orbital evolution is driven mainly by GW radiation [37–45]. More speculative evidence may come from rare high-energy transients. For example, a recently reported peculiar long-duration gamma-ray burst has been proposed to originate from the tidal disruption of a WD by an IMBH [46–49]. If these EM events are associated with WD-IMBH systems, they form a useful sample that can be used to verify the detectability of IMBHs by future GW observations.

To extract useful information from these potential EM counterparts, a self-consistent dynamical model for WD-IMBH interaction is required. Most existing models assume that the orbital evolution is driven primar-

* Contact author: xian.chen@pku.edu.cn

ily by GW radiation, while the EM emission is powered by the mass stripped from the WD and accreted onto the IMBH [27, 28, 32, 40, 41, 50–52]. However, compared to other compact objects such as neutron stars or stellar-mass BHs, the main difference of a WD lies in its relatively large size. Therefore, a test particle, as has been assumed in the aforementioned models, is insufficient to capture the rich dynamics induced by the tidal response of the WD. Indeed, models that include tidal heating of the WD and dissipation of the orbital energy do show results that deviate from pure test-particle evolution [25, 40, 53–55].

Despite the importance of tidal dissipation (TD), when dealing with the tidal force imposed on the WD, existing models commonly adopt the Newtonian prescription (e.g., [40, 54, 55]), even though the system may have already entered the regime of strong-gravity. For our interest, producing a GW signal with a high signal-to-noise ratio (SNR) requires the pericenter r_p of the WD-IMBH binary to lie within a few tens of the IMBH’s gravitational radius r_g [32, 56]. Therefore, we need a relativistic version of the TD model.

In a few exceptions, the relativistic tidal force is evaluated in a Fermi normal coordinate (FNC) frame that follows the motion of the WD [57, 58]. Hydrodynamical simulations performed in the FNC frame further indicate that the energy transfer during pericenter passage can differ substantially from the Newtonian prediction [59]. Nevertheless, owing to computational limitations, these simulations so far have not been able to follow the WD through multiple pericenter passages. The cumulative impact on the WD and the long-term evolution of the binary remains unclear, and hence the theoretical templates for joint EM and GW analyses still lack the necessary fidelity required to guide observations and extract reliable physical parameters.

To overcome this obstacle, we develop in this work a practical model of calculating the TD-induced energy and angular-momentum fluxes for a WD in the strong-gravity regime near an IMBH. We construct our model in the FNCs, to take advantage of the flatness of the spacetime in a local Lorentz frame, and calculate the fluxes according to the theory of gravity (g)-mode oscillation. The paper is organized as follows. We first outline the physical framework, quantitatively explaining the necessity of relativistic tidal fields, and summarize the key assumptions of our relativistic tidal model in Sec. II. In Sec. III, we develop a relativistic treatment of TD for highly eccentric WD-IMBH binaries and describe how the resulting energy and angular-momentum fluxes are incorporated into the orbital evolution. We then present the resulting evolution of the system in Sec. IV, where we also take into account the effects of IMBH spin. In Sec. V, we compute the GW emission including corrections due to relativistic TD, and evaluate the detectability of the TD effects in future GW observations. In Sec. VI, we discuss the implications of our results and outline potential directions for future extensions of this work.

II. CHARACTERISTIC SCALES

A. Domain of Relativistic Correction and Quadrupole Tide

The MT and TD processes of a WD around IMBH are often affected by strong general-relativistic (GR) effects [25–27, 32]. To identify the regime relevant to relativistic correction, we show in FIG. 1 the ratio between the tidal disruption radius (TDE radius), $r_t = R_*(M_\bullet/M_\star)^{1/3}$, and the gravitational radius, $r_g = GM_\bullet/c^2$, in the M_\star - M_\bullet parameter space. Here M_\bullet denotes the mass of the IMBH, while M_\star and R_\star are the mass and radius of the WD, respectively. The figure also shows the inferred locations of several observed QPEs [46, 60–63], whose physical parameters were obtained by fitting their light curves using the mass-transfer models, assuming highly orbital eccentricities [42, 49].

We find that when the IMBH mass exceeds $\sim 10^5 M_\odot$, the TDE radius will satisfy $r_t \lesssim 10 r_g$, indicating strong relativistic effects during the processes of tidal heating, mass transfer, or tidal disruption. In the same parameter space where $r_t/r_g \lesssim 10$, if the WD is more massive than $0.5 M_\odot$, such as a carbon–oxygen (CO) WD [64], the SNR of the GW radiation in the LISA band during an observational period of four years will exceed 10, as is indicated in FIG. 1 by the solid and dotted white curves (calculated following Refs. [65, 66]). Therefore, high-SNR GW events are highly relativistic as well. These findings imply that multi-messenger WD-IMBH systems discovered in the future by joint EM and GW observations will display significant GR effects.

The presence of GR effects complicates the calculation of the tidal force exerted by IMBHs on WDs. To approximate the tidal field, previous works often decompose the field around the WD into multipoles, starting from the quadrupole moment [53, 54, 67–70], and the relative contribution between adjacent multipoles scales with $R_\star/r_p \sim R_\star/r_t \sim (M_\star/M_\bullet)^{1/3}$. For WDs around an IMBH of $M_\bullet \gtrsim 10^4 M_\odot$, this ratio remains below 5%, indicating the predominance of the quadrupole moment. In FIG. 1, the black dot-dashed line corresponds to $R_\star/r_p = 5\%$. Above this line is the parameter space where the tidal field can be well approximated by a quadrupole. The majority of our interested systems lie in this region; therefore, we will derive only the quadrupole tidal field in the following.

The response of WD to an external tidal field is characterized by either gravity modes (g -modes) or fundamental ones (f -modes) [31, 53–55, 68]. The g -mode is important when the tidal-forcing frequency is lower than the stellar dynamical frequency $\omega_\star = \sqrt{GM_\star/R_\star^3}$, otherwise the f -mode dominates. To estimate the tidal-forcing frequency, which is the highest at the orbital pericenter, we introduce a dimensionless parameter $k = r_p/r_t$, so that the

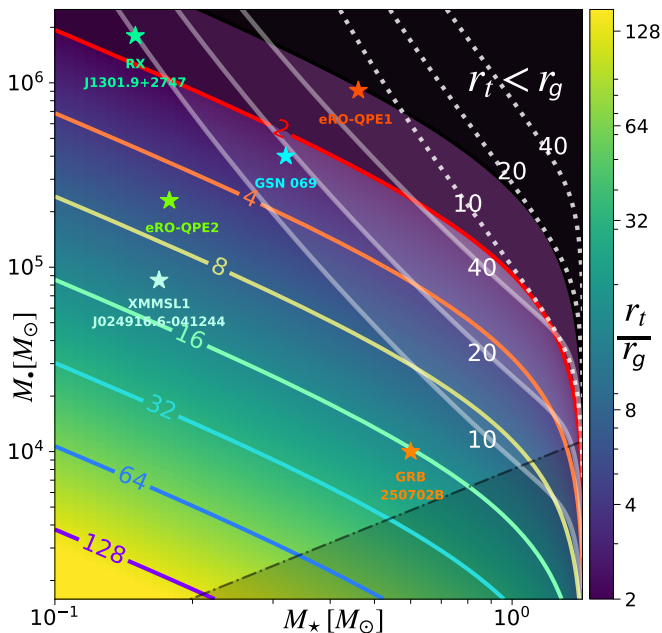


FIG. 1. Ratio of the Newtonian TDE radius of a WD, r_t , to the gravitational radius of an IMBH, r_g , shown in the M_\star - M_\bullet parameter space. The white lines indicate constant SNRs ($= 10, 20, 40$) for LISA observation, assuming a pericenter distance of $r_p = 2r_t$, a redshift of $z = 0.02$ ($d_L \simeq 85\text{Mpc}$), and an observation period of 4 years, whereas the solid and dotted line styles correspond to orbital eccentricities of $e = 0.95$ and $e = 0.99$, respectively. The region below the black dot-dashed line in the lower-right corner corresponds to $R_\star/r_t > 5\%$, where the assumption of quadrupole tidal field becomes invalid. The stars mark the inferred locations of a sample of QPEs.

instantaneous tidal frequency at the pericenter is

$$\omega_p = \omega_{\text{orb}} \sqrt{\frac{1+e}{(1-e)^3}} = \omega_\star \sqrt{\frac{1+e}{k^3}}, \quad (1)$$

where $\omega_{\text{orb}} = \omega_\star [(1-e)/k]^3/2$ is the mean orbital frequency. This relation suggests that g -mode oscillations dominate when the WD remains well outside the tidal disruption radius (e.g., $k \gtrsim 5$). In highly eccentric configurations with pericenter approaching the TDE radius, the orbital frequency near pericenter becomes comparable to the f -mode frequency, and f -mode excitation can in principle be significant. However, as will be demonstrated in Sec. IV, we find that such configurations are short-lived: once the pericenter enters this regime, rapid tidal dissipation efficiently circularizes the orbit and drives outward migration of the pericenter, quickly suppressing the resonance condition. Therefore, g -mode excitation captures the WD response over the majority of the parameter space considered in this work.

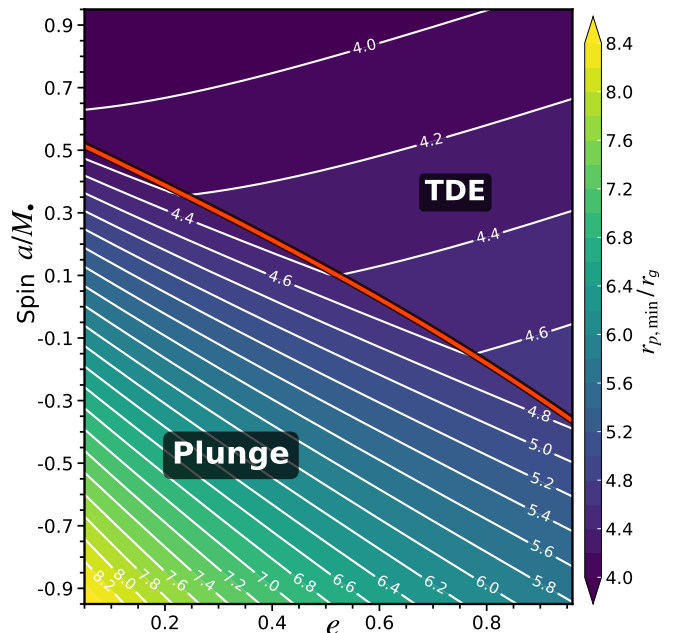


FIG. 2. Minimum allowed pericenter distance for a WD-IMBH system due to either relativistic plunge or tidal disruption, shown in the parameter space of IMBH spin a and orbital eccentricity e . The red line marks the points at which the critical plunge radius $r_{\text{plunge}}(a, e)$ equals the critical TDE radius $r_{\text{TDE}}(M_\star, M_\bullet, a, e)$. Therefore, in the lower-left region, $r_{\text{plunge}} > r_{\text{TDE}}$, and a WD will plunge into IMBH before tidal disruption. On the contrary, a WD in the upper-right region gets tidally disrupted before plunging. Here we have assumed $(M_\star, M_\bullet) = (0.6 M_\odot, 10^5 M_\odot)$.

B. Plunge Versus TDE

For the purposes of modeling a WD-IMBH system as well as predicting the observables, it is important to understand how the evolution terminates. Normally, the system ends up in a tidal disruption of the WD, or the WD plunging into the IMBH. In the Newtonian case, the outcome is determined by the masses of the WD and the IMBH [27, 32, 71, 72]. In the relativistic regime, however, the orbital parameters of the WD and the spin a of the IMBH¹ also matter, because they determine the existence and location of the inner-most turning point of a bound geodesic [73–77], as well as the tidal field felt by the WD in its rest frame [57, 59].

To simplify the problem, in the following we will restrict the WD orbit in the equatorial plane of the spinning IMBH. In this case, given the spin a , a secular orbit admits two radial turning points, corresponding to the pericenter and apocenter, with radial coordinates r_p and r_a [73]. Then, following Ref. [74], we can characterize

¹ Note that a denotes the Kerr spin parameter and should not be confused with the orbital semi-major axis.

such a relativistic orbit with two parameters, r_p as is defined above and the eccentricity $e \equiv (r_a - r_p)/(r_a + r_p)$.

With this, we can now determine the outcome of a relativistic WD-IMBH inspiral. This is done by fixing the orbital eccentricity e and calculating the critical pericenter distances, $r_{\text{plunge}}(a, e)$ and $r_{\text{TDE}}(M_\star, M_\bullet, a, e)$, below which plunge and TDE, respectively, will occur. The larger one of these two pericenter distances determines the actual fate of the system, setting the minimum allowed distance between the WD and the IMBH to be

$$r_{p,\text{min}}(M_\star, M_\bullet, a, e) = \max(r_{\text{plunge}}, r_{\text{TDE}}). \quad (2)$$

Here, we have used a relativistic tidal tensor [78–80] to find r_{TDE} , and more details are given in Section III. Notice the different between r_{TDE} and r_t , the latter of which does not depend on a or e .

FIG. 2 shows the minimum pericenter distance defined by Eq. (2) in the $e - a$ parameter space, where negative values of the spin a corresponds to retrograde orbits. This shows the impact of a and e on the outcome, even when the masses, (M_\star, M_\bullet) , are both fixed.

In particular, given e , we find $r_{p,\text{min}}$ decreases with increasing BH spin in both the plunge region and the TDE region. This anti-correlation reflects how BH spin reshapes both the angular-momentum barrier of equatorial geodesics and the strength of relativistic tidal field. For prograde orbits, frame dragging lowers the effective angular-momentum barrier, allowing a given pericenter distance to be reached with smaller specific angular momentum and orbital energy, thereby shifting the plunge separatrix inward [73, 74]. Simultaneously, the anti-correlation between the relativistic tidal tensor and the spin parameter weakens the tidal stretching at fixed r_p , so that tidal disruption requires deeper penetration into the gravitational potential. For retrograde orbits, both effects act in the opposite direction, shifting the plunge and TDE thresholds outward.

The contour spacing in FIG. 2 also suggests that as the IMBH spin increases, angular-momentum barrier shrinks much faster than the relativistic tidal tensor weakens. As a result, increasing a will eventually put the WD-IMBH in the TDE regime. For this reason, for a $0.6M_\odot$ WD around a 10^5M_\odot IMBH, the outcome is always a TDE when $a \gtrsim 0.5M_\bullet$. On the contrary, when $a \lesssim -0.3M_\bullet$, the result is plunge.

C. Gravitational Radiation Versus Tidal Dissipation

From the entry into the relativistic regime until its termination by tidal disruption or plunge, the evolution of a WD-IMBH binary is driven mainly by GW radiation and tidal interaction. While GW radiation extracts energy and angular momentum from the binary orbit [81, 82], tidal interaction leads to excitation and damping of stellar oscillation modes, nonlinear tidal responses, or shock heating in the outer layers of the WD [68, 83], thereby

irreversibly dissipating orbital energy and angular momentum into internal motions, heating, and spin of the WD [67]. The relative importance of GW radiation and TD can be evaluated by their respective characteristic timescales [54].

For example, GW radiation extracts orbital angular momentum J_{orb} at a rate of

$$t_{\text{GW}} = \frac{J_{\text{orb}}}{|\dot{J}_{\text{GW}}|} = \frac{5}{32} \frac{GM_\bullet}{c^3} \frac{q^{5/3} k^4}{\mathcal{C}_\star^4 (1-e)^{3/2}} \frac{(1+e)^{5/2}}{(1+7e^2/8)}, \quad (3)$$

where $q = M_\star/M_\bullet \sim 10^{-6}$ is the mass ratio of the binary, $\mathcal{C}_\star = GM_\star/R_\star c^2 \sim 10^{-4}$ is the compactness of WD, and we have followed Refs. [54, 68] to express the angular-momentum loss rate \dot{J}_{GW} . The characteristic timescale associated with TD is

$$t_{\text{tide}} = \frac{J_{\text{orb}}}{|\dot{J}_{\text{tide}}|} = \frac{GM_\bullet}{c^3} \frac{q^{1/3} k^{13/2}}{\mathcal{C}_\star^{3/2} \dot{\mathcal{J}} (1-e)^{3/2}} (1+e)^{5/2} \quad (4)$$

[54], where $\dot{\mathcal{J}} \sim 10^{-6}$ for $k \sim \mathcal{O}(1)$ is the dimensionless tidal angular momentum transfer rate $\dot{\mathcal{J}}(k, e)$.

The ratio of the two timescales for high eccentricity is therefore

$$\frac{t_{\text{GW}}}{t_{\text{tide}}} = \frac{q^{4/3} \dot{\mathcal{J}}}{\mathcal{C}_\star^{5/2} k^{5/2}} \frac{5/32}{(1+7e^2/8)} \propto \dot{\mathcal{J}}(k) r_p^{-5/2}. \quad (5)$$

TD becomes important when this ratio is not much smaller than unity. In our problem, since both q and $\dot{\mathcal{J}}$ are extremely small, significant TD appears at $r_p/r_g \lesssim 10$, corresponding to $k \lesssim 3$. This estimation indicates that a WD in the most relativistic regime of an IMBH is also experiencing strong TD. We find a similar conclusion if we use orbital energy, instead of angular momentum, to do the evaluation.

III. RELATIVISTIC TIDAL DISSIPATION

A. Relativistic Tidal Field

The formulation of a TD theory in the strong-gravity regime must begin with a rigorous relativistic treatment of the tidal force, which we briefly review in this subsection. The most natural coordinate system in which this force can be expressed is a local, freely-falling reference frame comoving with the center-of-mass of the WD. In fact, this is how the FNCs are introduced [57, 58, 84].

To understand the definition of FNCs, we first describe the spacetime around a spinning IMBH. In Boyer–Lindquist coordinates (BLCs) $x_{\text{BLC}}^\mu = (t, r, \theta, \phi)$ and using geometrized units, the metric takes the form

$$ds^2 = - \left(1 - \frac{2M_\bullet r}{\Sigma}\right) dt^2 - \frac{4M_\bullet a r \sin^2 \theta}{\Sigma} dt d\phi + \frac{\Sigma}{\Delta} dr^2 + \Sigma d\theta^2 + \frac{(r^2 + a^2)^2 - \Delta a^2 \sin^2 \theta}{\Sigma} \sin^2 \theta d\phi^2 \quad (6)$$

[85], where $\Sigma = r^2 + a^2 \cos^2 \theta$ and $\Delta = r^2 + a^2 - 2M_\bullet r$. Notice that geodesic motion in this spacetime admits three constants of motion (E, L_z, Q), which are the specific energy, z -angular momentum, and Carter constant, respectively [86]. They will be used to construct the FNCs and the corresponding tidal tensor.

To relate vectors and tensors in different coordinate systems, orthonormal tetrads are often introduced. In BLCs, the tetrad bases are $e^{(a)} = e_\mu^{(a)} \mathbf{d}x_{\text{BLC}}^\mu$, while in FNCs the corresponding bases are $\Lambda^{(a)} = \Lambda_\alpha^{(a)} \mathbf{d}x_{\text{FNC}}^\alpha$. In both cases, $(a) = 0, 1, 2, 3$ are the tetrad indices and $\mathbf{d}x^\mu$ denotes the coordinate one-form. We further denote the FNC coordinates as $x_{\text{FNC}}^\alpha = (\tau, x^1, x^2, x^3)$ to distinguish them from the BLCs, and hence τ is the proper time along the reference geodesic. Explicit expressions for the tetrad components $e_\mu^{(a)}$ and $\Lambda_\alpha^{(a)}$ can be found in Refs. [57, 58]. Here, we emphasize the relation $\partial x_{\text{BLC}}^\mu / \partial x_{\text{FNC}}^\alpha = \Lambda_\alpha^{(a)} e_{(a)}^\mu$. Based on it, the transformation of tensor in different coordinates can be performed. For example, the Riemann tensor transforms as

$$R_{\alpha\beta\gamma\delta}^{\text{FNC}} = \Lambda_\alpha^{(a)} \Lambda_\beta^{(b)} \Lambda_\gamma^{(c)} \Lambda_\delta^{(d)} e_{(a)}^\mu e_{(b)}^\nu e_{(c)}^\kappa e_{(d)}^\lambda R_{\mu\nu\kappa\lambda}^{\text{BLC}}, \quad (7)$$

where $R_{\mu\nu\kappa\lambda}^{\text{BLC}}$ is determined by the Boyer-Lindquist metric given in Eq. (6).

From the Riemann tensor in the FNCs, one can derive the tidal tensor. In the following analysis, we will only keep the leading order terms. Higher-order tidal corrections arise from higher-order terms in the FNC metric expansion, and involve covariant derivatives of the curvature tensor as well as nonlinear curvature couplings [58], and hence they can be neglected for the reasons discussed in Sec. II A. Moreover, we will restrict our analysis to a simple configuration: a WD in the equatorial plane of a Kerr IMBH. In this case, high-order relativistic effects such as spin-orbit and spin-spin couplings [87–89] can be neglected, and the rotation of the WD does not introduce additional significant dynamical effects in the FNCs. With these simplifications, the relativistic quadrupole tidal tensor C_{ij} in the rest frame of the WD's center-of-mass is

$$\begin{aligned} C_{11} &= \frac{M_\bullet}{r^3} \left[(1 - 3 \cos^2 \Psi) - \frac{3\mathcal{L}}{r^2} \cos^2 \Psi \right], \\ C_{12} = C_{21} &= -\frac{3M_\bullet}{r^3} \left(1 + \frac{\mathcal{L}}{r^2} \right) \sin \Psi \cos \Psi, \\ C_{22} &= \frac{M_\bullet}{r^3} \left[(1 - 3 \sin^2 \Psi) - \frac{3\mathcal{L}}{r^2} \sin^2 \Psi \right], \\ C_{33} &= \frac{M_\bullet}{r^3} \left(1 + \frac{3\mathcal{L}}{r^2} \right), \end{aligned} \quad (8)$$

where $\mathcal{L} = (L_z - aE)^2$. Notice that in this work, the FNC basis vectors labeled by indices 1 and 2 lie in the equatorial plane, whereas in Refs. [57–59] the equatorial plane aligns with the 1 and 3 directions. We make this modification because it allows the tidal field to be expressed more compactly in terms of spherical harmonics.

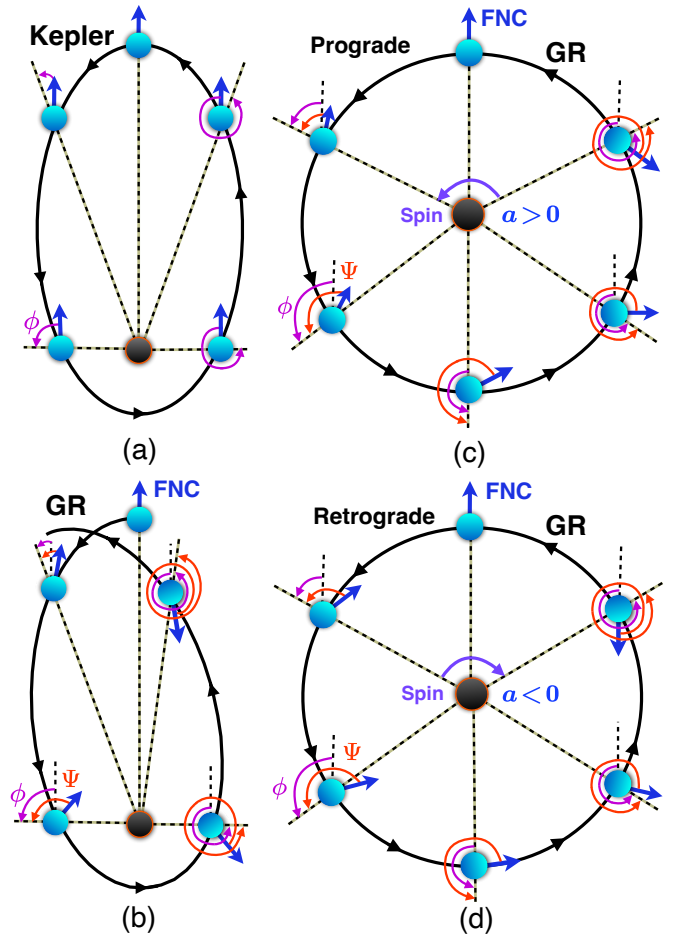


FIG. 3. Orientation of the Fermi normal coordinates for a WD on (a) an eccentric Newtonian orbit, (b) an eccentric orbit around a Schwarzschild IMBH, (c) a prograde circular orbit in the equatorial plane of a Kerr IMBH, and (d) a retrograde circular orbit in the equatorial plane of a Kerr IMBH. In each panel, the blue arrow represents the tetrad vector $\Lambda^{(1)}$. The azimuthal angle ϕ in the Boyer-Lindquist coordinates and the rotational angle Ψ associated with the Fermi-normal coordinates are also marked.

The tensor components in Eq. (8) depend explicitly on the rotation angle Ψ , which specifies the orientation of the parallel-transported FNC frame relative to the BLC basis [57]. Its geometrical meaning is illustrated in FIG. 3. In the Newtonian limit, the local inertial frame remains aligned with the instantaneous radial direction, so that Ψ coincides with the orbital phase, $\Psi = \phi$ (panel a). By contrast, in GR, the FNC tetrad undergoes non-trivial parallel transport along the geodesic. For eccentric geodesic motion in Schwarzschild spacetime (panel b), spacetime curvature causes the parallel-transported FNC tetrad to undergo a cumulative rotation along the orbit. This rotation proceeds in the opposite sense to the relativistic apsidal advance of the geodesic. When the central IMBH is spinning (panels c and d), frame dragging further modifies the evolution of Ψ . The resulting

rotation depends on the relative orientation of the orbital angular momentum and the BH spin: for prograde orbits the accumulated rotation of the parallel-transported FNC tetrad is partially suppressed, whereas for retrograde orbits it is enhanced.

This additional rotation occurring in the regime of strong gravity, together with the apsidal precession of eccentric orbit, implies that the orientation of the tidal-tensor principal axes, evaluated at successive pericenter passages, is not fixed in the WD comoving frame. This variation changes the phase of the tidal forcing, so that it no longer repeats modulo 2π . Consequently, the coherence between tidal forcing and stellar mode, which may establish in the Newtonian case, will be broken in the relativistic regime. The efficiency of energy and angular-momentum exchange between the WD and the binary orbit is, therefore, fundamentally altered.

B. Tidal Response of White Dwarf

While the construction of the tidal tensor requires a relativistic treatment, the tidal response of the WD can be described within Newtonian theory, as the spacetime in the FNCs is nearly flat and the WD itself is weakly relativistic. As discussed earlier, the excitation and dissipation of gravity waves govern the evolution of the WD–IMBH system prior to mass transfer or tidal disruption. This is supported by the fact that the tidal-forcing frequency is much lower compared to the Brunt–Väisälä frequency, N , and the Lamb frequency, L_l [90].

In this regime, earlier Newtonian analyses [54, 68, 83, 91] have shown that oscillations are confined to the outer layers of the WD and rapidly reach large amplitudes, such that the condition for nonlinear wave breaking is satisfied. These waves dissipate their energy locally before reflecting to form normal-mode patterns, rendering a normal-mode analysis of the WD in our problem not only impractical but also physically inappropriate.

A more appropriate model is a forced wave-propagation problem, in which gravity waves are continuously excited by the time-dependent tidal potential, carrying energy and angular momentum outward into the stratified envelope. Under the condition $\omega^2 \ll N^2, L_l^2$, the response of the WD is well captured by the standard WKB dispersion relation, as studied in Refs. [68, 83].

In their work, a specific tidal force $\mathbf{a}_{\text{tidal}}$ is imposed on the WD, and the response is quantified by the Lagrangian displacement $\boldsymbol{\xi}$, expressed in spherical coordinates (R, ϑ, φ) . To solve the problem, both the displacement and the driving force are first decomposed into vector spherical harmonics $\mathbf{Y}_{lm}^{\text{R,S,T}}$, where the superscripts R, S, and T label the radial, spheroidal, and toroidal vector spherical harmonic basis functions, respectively [92].

One then writes

$$\begin{aligned} \boldsymbol{\xi} &= \sum_{lm} (\xi_{lm}^{\text{R}} \mathbf{Y}_{lm}^{\text{R}} + \xi_{lm}^{\text{S}} \mathbf{Y}_{lm}^{\text{S}} + \xi_{lm}^{\text{T}} \mathbf{Y}_{lm}^{\text{T}}), \\ \mathbf{a}_{\text{tidal}} &= \sum_{lm} (F_{lm}^{\text{R}} \mathbf{Y}_{lm}^{\text{R}} + F_{lm}^{\text{S}} \mathbf{Y}_{lm}^{\text{S}} + F_{lm}^{\text{T}} \mathbf{Y}_{lm}^{\text{T}}), \end{aligned} \quad (9)$$

where the expansion coefficients depend on the radial coordinate R and the proper time τ .

Since the coefficients are time-dependent, they are further decomposed into Fourier series, $F_{lm}^{\text{R,S,T}}(R, \tau) = \sum_n F_{nlm}^{\text{R,S,T}}(R) e^{-i\omega_{nlm}\tau}$. The solution for each mode, i.e., $\xi_{nlm}^{\text{R,S,T}}$, can then be obtained by solving a Schrödinger-like wave equation²

$$Z''_{nlm} + k_{nlm}^2 Z_{nlm} = \chi_{nlm}^{-1/2} \frac{l(l+1)}{\omega_{nlm}^2} N^2 V_{nlm}(R), \quad (10)$$

where $Z_{nlm}(R) := \chi_{nlm}^{-1/2} R^2 \xi_{nlm}^{\text{R}}$ is a rescaled radial displacement variable, $V_{nlm}(R)$ is a source term associated with the driving force, primes denote derivatives with respect to R , and k_{nlm} is a function of R .

Given the decomposition in Eq. (9), the source term $V_{nlm}(R)$ can be written in terms of the force components as

$$\begin{aligned} V_{nlm}(R) &= \frac{F_{nlm}^{\text{R}}}{N^2} \left(1 - \frac{\omega_{nlm}^2}{L_l^2} \right) - \frac{(F_{nlm}^{\text{S}} R)'}{N^2} \\ &+ F_{nlm}^{\text{S}} \left[\frac{R}{g} + \frac{1}{N^2} \frac{2\omega_{nlm}^2}{L_l^2 - \omega_{nlm}^2} \left(\frac{d \ln c_s^2}{d \ln R} - 2 \right) \right], \end{aligned} \quad (11)$$

where all background quantities, $g = -P'/\rho$, $c_s^2 = (\partial P / \partial \rho)_s$, $N^2 = g^2(\rho'/P' - 1/c_s^2)$, and $L_l^2 = l(l+1)c_s^2/R^2$ are defined with respect to an unperturbed, spherically symmetric WD structure.

In our problem, the WD–IMBH binary is not necessarily circular, and multiple frequencies ω_{nlm} naturally arise when we consider eccentric orbits. In addition, we compute $\mathbf{a}_{\text{tidal}}$ using the tidal tensor C_{ij} given in Eq. (8) (see also Eqs. 127–134 in Ishii *et al.* [58]). We then derive the coefficients required to express the tidal force and the displacement field. For example, to leading order we find

$$\begin{aligned} F_{2m}^{\text{S}}(R, \tau) &= -\Phi_{2m}/R = \sum_n F_{n2m}^{\text{S}}(R) e^{-i\omega_{n2m}\tau} \\ &= \frac{GM_\bullet}{r^3} \left(1 + \frac{\mathcal{L}}{r^2} \right) W_{2m} e^{-\text{sgn}(m) 2i\Psi} R, \end{aligned} \quad (12)$$

where $W_{2\pm 2} = \sqrt{3\pi/10}$, $W_{20} = \sqrt{\pi/5}$, and $W_{2\pm 1} = 0$. Here, Φ_{2m} denotes the leading-order coefficient in the

² The other displacement components, $\xi_{nlm}^{\text{S,T}}$, satisfy equations of similar form [68]. Under the WKB approximation, the spheroidal component is related to the radial displacement by $\xi_{nlm}^{\text{S}} \simeq -i\xi_{nlm}^{\text{R}} k_{nlm} R / [l(l+1)]$.

spherical-harmonic expansion of the tidal scalar potential, $\Phi_{\text{tidal}} \simeq \sum_m \Phi_{2m} Y_{2m}$, and is related to C_{ij} via the symmetric-trace-free spherical tensor harmonics [93]. Our expression for Φ_{2m} reproduces the classical Newtonian result of Press and Teukolsky [67], for which $F_{2\pm 1}^S$ vanishes. This follows directly from our choice $C_{23} = C_{32} = 0$ in Eq. (8).

One interesting consequence is worth noting. Since both r and Ψ are functions of the proper time τ , Eq. (12) implies that the tidal forcing consists of harmonics associated with two distinct frequencies: the radial orbital frequency and the azimuthal frequency. This represents a qualitative departure from the Keplerian case, in which only a single frequency is present.

We further note that, in the outer WD envelope, $\omega_{nlm}^2 \ll N^2, L_l^2$. In this regime, the WKB approximation applies, and χ_{nlm} , k_{nlm}^2 , and V_{nlm} reduce to

$$\begin{aligned} \chi_{nlm}(R) &\simeq \frac{l(l+1)}{\rho \omega_{nlm}^2}, & k_{nlm}^2(R) &\simeq \frac{l(l+1)}{R^2 \omega_{nlm}^2} N^2, \\ V_{nlm}(R) &\simeq \frac{F_{nlm}^S R}{g} + \frac{F_{nlm}^R - (F_{nlm}^S R)'}{N^2}. \end{aligned} \quad (13)$$

Here k_{nlm}^2 is positive definite, indicating a propagating-wave regime. Moreover, imposing the physical boundary condition that no waves enter from the stellar surface (or from infinity), the above solution corresponds to a wave that transports energy outward. A further simplification follows from our earlier observation that only the quadrupole ($l = 2$) component contributes to the tidal tensor. In this case, the radial and spheroidal components of $\mathbf{a}_{\text{tidal}}$ satisfy $F_{nlm}^R \approx (F_{nlm}^S R)'$. Substituting this relation into Eq. (13) yields $V_{nlm} \simeq F_{nlm}^S R/g$.

C. Energy and Angular-momentum Fluxes

Having derived the tidal response of the WD (e.g., ξ_{nlm}^R), we can compute the energy and angular momentum extracted from the binary orbit and deposited into the WD. From these quantities, the corresponding back reaction on the binary orbit can be inferred. We compute the z -component of the time-averaged angular-momentum flux carried by tidally excited gravity waves by

$$\begin{aligned} \dot{L}_z(R) &= \left\langle \oint \rho R^3 [\mathbf{e}_z \cdot (\mathbf{e}_R \times \mathbf{v})] (\mathbf{v} \cdot \mathbf{e}_R) d\Omega \right\rangle_\tau \\ &\simeq \frac{\rho R^3}{2N} \sum_{nlm}^{m>0} \frac{m k_{nlm}^2 R^2}{[l(l+1)]^{3/2}} |\omega_{nlm}|^3 |\xi_{nlm}^R|^2 \end{aligned} \quad (14)$$

[54, 68], where $\langle \dots \rangle_\tau$ denotes averaging over proper time, and $\mathbf{v} = \partial \boldsymbol{\xi} / \partial \tau$ is the fluid velocity measured in the FNCs, i.e., the three-velocity in the FNCs.

The result depends on the FNC radial coordinate R , whose evaluation requires some care (see also Ref. [68]). In the gravity-wave model, the WD interior is divided

into two regions. From the core to a radius R_b , gravity waves propagate both inward and outward, whereas from a slightly larger radius R_a to the stellar surface the waves propagate only outward. The radii R_a and R_b , being close to each other, typically coincide with a sharp chemical-composition gradient, across which the Brunt–Väisälä frequency varies rapidly and satisfies $N_a^2 \gg N_b^2$.

The angular momentum flux reaches an approximately constant value near this transition region and evolves only weakly in the outer layers. We therefore evaluate the net angular-momentum flux at R_a , i.e., $\dot{L}_z(R_\star) \sim \dot{L}_z(R_a)$ [68]. Assuming that the outward-propagating gravity-waves are efficiently damped in the outer layers, the angular-momentum flux is irreversibly absorbed by the WD and is therefore equal to the change rate of the orbital angular momentum, i.e., $\langle dL_z/d\tau \rangle_\tau \sim \dot{L}_z(R_\star)$.

Using the tidal response ξ_{nlm}^R obtained in Eq. (10), the orbit-averaged rate of change of L_z can be expressed entirely in terms of the tidal forcing and the internal structural properties of the WD. In practice, the calculation is carried out using dimensionless quantities,

$$\left\langle \frac{dL_z}{d\tau} \right\rangle_\tau \simeq \mathcal{C}_\star^{-1} \sum_{nlm}^{m>0} m \mathcal{F}_{lm}(\tilde{F}_{nlm}^S, \tilde{\omega}_{nlm}), \quad (15)$$

where \mathcal{C}_\star is the compactness of the WD, and

$$\begin{aligned} \mathcal{F}_{lm}(\tilde{F}_{nlm}^S, \tilde{\omega}_{nlm}) &= \frac{\hat{f}}{[l(l+1)]^{5/2}} \left(\frac{R_\star}{r_g} \right)^{2l} \times \\ &\tilde{R}_a^{2l-4} \left| \tilde{F}_{nlm}^S(\tilde{R}_a) \right|^2 |\tilde{\omega}_{nlm}|^5. \end{aligned} \quad (16)$$

Here, quantities with tildes denote the corresponding dimensionless variables. In particular, $\tilde{F}_{nlm}^S = F_{nlm}^S(R_a/r_g)^{1-l} (GM_\bullet/c^4)$, with $\tilde{R}_a = R_a/R_\star \sim 0.8$, and $\tilde{\omega}_{nlm} = \omega_{nlm}/\omega_\star$. The dimensionless coefficient \hat{f} depends only on the internal structure of the WD and must be calibrated using detailed numerical calculations. For a typical $0.6M_\odot$ WD, numerical studies find $\hat{f} \sim 10^2$ [54, 68, 91].

The time-averaged energy dissipation rate can also be expressed in terms of the same function \mathcal{F}_{lm} ,

$$\left\langle \frac{dE}{d\tau} \right\rangle_\tau \simeq \frac{\mathcal{C}_\star^{1/2}}{q} \sum_{nlm}^{m>0} |\omega_{nlm}| \mathcal{F}_{lm}(\tilde{F}_{nlm}^S, \tilde{\omega}_{nlm}). \quad (17)$$

Unlike the angular-momentum flux, the energy dissipation receives contributions from axisymmetric ($m = 0$) modes. This is because axisymmetric perturbations do not exert a net torque, but they do perform net work.

The dissipation rates derived above are formulated in the FNCs and are referenced to the proper time τ . However, orbital evolution is conventionally described in the BLCs. To relate the two rates, we use

$$\frac{\langle dE/dt \rangle_t}{\langle dE/d\tau \rangle_\tau} = \frac{\langle d\tau/d\lambda \rangle_\lambda}{\langle dt/d\lambda \rangle_\lambda} = \frac{\langle \Sigma \rangle_\lambda}{\Upsilon_t}, \quad (18)$$

where λ is the Mino time, $\langle \Sigma \rangle_\lambda = \Lambda_r^{-1} \int \Sigma d\lambda$, and $\Upsilon_t = T_r/\Lambda_r$, with Λ_r and T_r denoting the radial periods in Mino time and coordinate time, respectively [94, 95].

The introduction of the Mino time is essential for mitigating the slow convergence of Fourier expansions, such as that encountered in Eq. (12), particularly for highly eccentric orbits. In this work, we implement a two-step frequency-domain method based on the Mino time. The key idea is to first express the tidal factors as a Fourier series with respect to the Mino time λ . The corresponding fundamental frequencies for $1/r$ and $e^{\pm i\Psi}$ are simply $\Omega_r = 2\pi/\Lambda_r$ and $\Omega_\Psi = \langle d\Psi/d\lambda \rangle_\lambda$, respectively [95–97]. We then re-expand the result by expressing the Mino time itself as a Fourier series in the proper time τ , namely, $\lambda = \tau/\langle \Sigma \rangle_\lambda + \sum_k C_k \exp[-ik\Omega_r\tau/\langle \Sigma \rangle_\lambda]$. This procedure naturally leads to products of finite Fourier series, which we evaluate numerically using discrete convolution. As a result, the Fourier expansion can be computed efficiently to high harmonic orders.

IV. RESULTS

A. Orbital Evolution Around Non-Spinning IMBH

Using the prescription for TD developed above, we first study the orbital evolution of a WD around a non-spinning IMBH. In addition to TD, GW radiation is another important driver of the orbital evolution. However, the standard PN formalism is inadequate for accurately capturing the dynamics of our system, which resides deep in the strong-gravity regime. Therefore, we adopt black hole perturbation theory (BHPT) to compute energy and angular-momentum loss due to GW radiation for stable, bound, equatorial Kerr orbits. Specifically, for orbits with eccentricities in the range $0 \leq e \leq 0.85$, we rely on the publicly available GW flux data set `FastEMRIWaveforms` [98–101]. For more eccentric trajectories with $0.85 \leq e \leq 0.96$, we perform direct BH perturbation calculations using `pybhpt` [102, 103].

FIG. 4 shows the evolution in the $e - r_p$ parameter space of a WD orbiting an IMBH under the combined effects of gravitational radiation and TD. The color map indicates the pericenter evolution rate \dot{r}_p . Solid curves denote secular trajectories including both mechanisms, while dashed curves show the evolution driven solely by GW emission. The separation between the two sets of curves signals a transition in the dominant dissipation mechanism. For sufficiently large pericenter distances ($r_p \gtrsim 3r_t$), the solid and dashed curves nearly overlap, indicating that TD is negligible compared to GW radiation. By contrast, at smaller pericenter distances ($r_p \lesssim 2r_t$), the two curves deviate, demonstrating that TD becomes dynamically important.

A noteworthy feature is the existence of a region bounded by the condition $\dot{r}_{p,\text{GW}} + \dot{r}_{p,\text{TD}} = 0$ (e.g., the yellow markers). Below this boundary, r_p increases with time. This behavior is qualitatively distinct from GW-

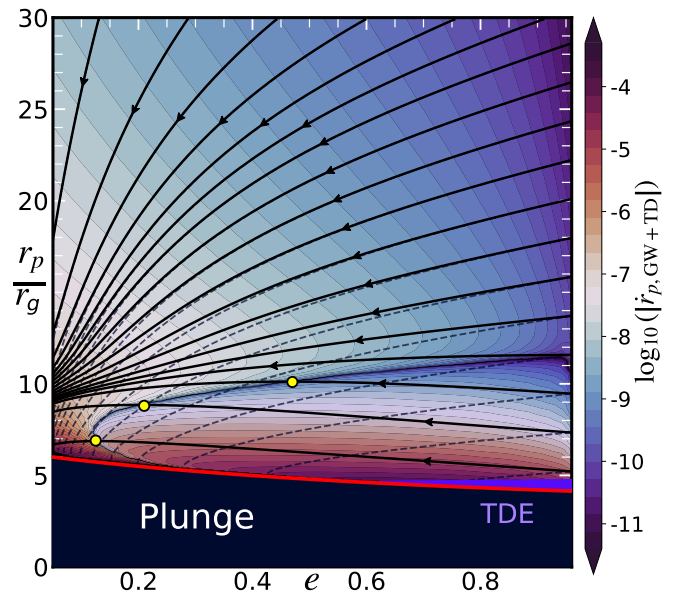


FIG. 4. Orbital evolution streamlines in the $e - r_p$ parameter space for a WD orbiting a non-spinning IMBH under the combined effects of gravitational radiation and TD. Solid curves show orbital trajectories when both mechanisms are included, while dashed curves correspond to evolution driven solely by gravitational radiation. The color map encodes the pericenter evolution rate $\log_{10}(|\dot{r}_{p,\text{GW}} + \dot{r}_{p,\text{TD}}|)$ under two effects, where $\dot{r}_p = (dr_p/dt)/c$. The region below the red curve indicates the plunge region, defined by $r_p < r_{p,\text{plunge}}$, where the orbit directly falls into the IMBH event horizon. The purple strip adjacent to the red curve denotes the TDE region, defined by $r_{p,\text{plunge}} < r_p < r_t$. Yellow dots mark the locations along the streamlines where the pericenter distance r_p reaches a maximum. In this plot, we assume $M_\star = 0.6 M_\odot$ and $M_\bullet = 10^5 M_\odot$.

driven binaries, for which r_p decreases monotonically. Detecting such a signature in GW or EM observations would provide direct evidence that TD is taking place in WD-IMBH binaries. As the binaries evolve past this boundary toward lower eccentricities, GW emission again dominates and drives a decrease in r_p .

The origin of this non-monotonic behavior can be understood from the relation $r_p = p/(1+e)$. Although TD reduces both the semi-latus rectum p and the eccentricity e , the fractional decrease in eccentricity dominates, i.e., $|\dot{p}/p| < |\dot{e}/(1+e)|$. As a result, the reduction in e outweighs the shrinkage of p , leading to an increase in r_p despite the overall orbital decay.

FIG. 4 also shows that the inclusion of TD can substantially alter the outcome of binary evolution. First, the solid streamlines show that WD-IMBH binaries are mostly circularized ($e = 0$) when TD is included. In contrast, the dashed streamlines indicate that, in the absence of TD, many systems remain eccentric by the time they either plunge or undergo tidal disruption. Second, those binaries that would enter the TDE region if GW radiation is the sole driving mechanism (e.g., the lowest

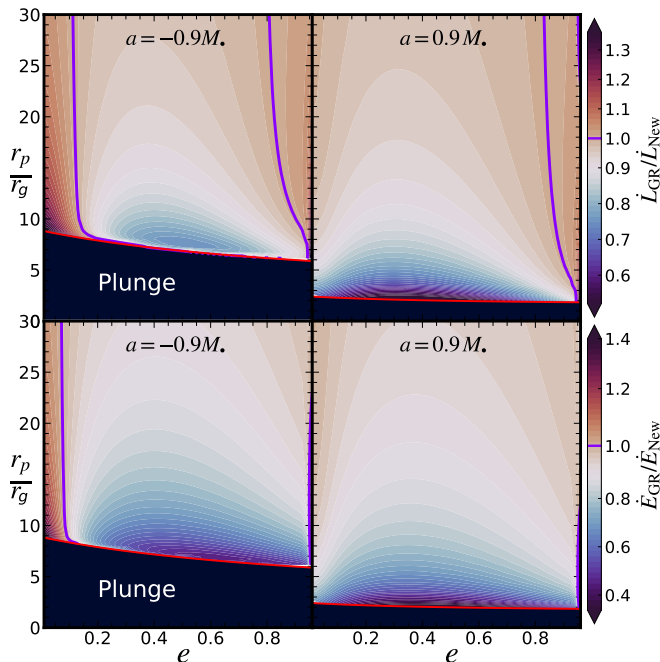


FIG. 5. Comparison of the TD-induced angular-momentum (upper panels) and energy (lower panels) loss rates computed in the Newtonian and full GR cases. The color maps show the ratios of the rates obtained in the two cases, and the purple curves mark the loci where the ratio equals unity. The left and right panels correspond to IMBH spins $a = -0.9M_\bullet$ and $a = 0.9M_\bullet$, respectively. All other parameters are the same as those in FIG. 4.

dashed streamline), now with TD, end up in the plunge region. These TD-induced differences would affect the predictions for and interpretations of future GW and EM observations, as we will discuss in Sec. VI.

B. Impact of IMBH Spin

The spin of IMBH shifts the boundary between TDE and plunge orbits, changes the strength of the tidal field, and induces extra rotation of the FNCs, as discussed in Secs. II B and III A. FIG. 5 shows how these effects modify the TD rates of energy and angular momentum in a WD–IMBH binary. The rates shown here are normalized by their Newtonian counterparts in order to highlight the importance of GR corrections. The Newtonian rates are obtained by evaluating the same expressions in Eq. (12) in the Keplerian limit, where relativistic precession is absent.

We find that, over most of the $e - r_p$ parameter space, the orbit-averaged relativistic TD rates are systematically suppressed relative to their Newtonian counterparts. We emphasize that this suppression does not arise from a weaker instantaneous tidal field. On the contrary, near pericenter, the instantaneous relativistic tidal field can exceed the Newtonian one. The reduction in the net

dissipation is a consequence of the loss of temporal coherence in the tidal forcing, induced by the rotation of the FNCs, as discussed in Sec. III A.

This interpretation is further corroborated by a comparison between the prograde and retrograde cases shown in FIG. 5. For a given pericenter distance with $r_p \lesssim 15 r_g$, the suppression of the TD rates is more pronounced for retrograde orbits than for prograde ones. Retrograde orbits, as shown in Sec. III A, experience a larger effective frame-rotation rate of the FNCs. Therefore, the loss of phase coherence in the tidal forcing is stronger, leading to a more prominent suppression of the TD rates.

The trend reverses in the limit of extreme eccentricities, e.g., at $e \simeq 0$ as well as $e \simeq 1$, where we find an enhancement of the TD rates in the GR case. This enhancement can be understood as follows. When $e \simeq 0$, the separation between the WD and the IMBH varies weakly, so that the FNC frame undergoes approximately uniform rotation. This shifts the tidal forcing to higher frequencies, which, according to Eq. (16), generally enhances the stellar response. When $e \simeq 1$, although we also find a clear enhancement of the TD-induced angular-momentum loss rates in the GR case, the underlying physical mechanism is not yet fully understood. A possible contributing factor is that the sharp pericentre passage leads to highly non-uniform tidal forcing, thereby broadening the effective frequency spectrum, with relativistic effects potentially further amplifying this behavior.

Having understood the impact of spin on the TD rates, we can now study the long-term evolution of a WD around a spinning IMBH. We notice that the spin-dependent effects enter primarily through the conserved quantity $\mathcal{L} = (L_z - aE)^2$, e.g., in Eq. (12). If $r_p \gg r_g$, we have $L_z/M_\bullet \gg E$, and the spin effect will be insignificant. Therefore, spin becomes important in the strong-gravity regime, where r_p is not much larger than r_g . Such a dependence is shown in FIG. 6, where we plot representative trajectories for two extreme spin values, $a = \pm 0.9M_\bullet$. Large deviation between prograde and retrograde orbits is seen only at $r_p \lesssim 16 r_g$.

During the spin-dependent evolution, as e decreases and the binary circularizes, a prograde orbit (solid curve) most of the time remains at a larger pericenter distance r_p than a retrograde orbit (dashed curve) of the same e . This general trend is a consequence of two effects operating in different regimes.

First, in the regime where GW radiation dominates the orbital evolution—corresponding to the region above the boundary marked by the yellow (blue) dots in FIG. 6—prograde orbits radiate less GW energy and angular momentum than retrograde ones [74]. As a result, their orbital shrinkage (tendency to drift downward) is slower.

Second, in terms of losing energy via TD, prograde orbits lose orbital energy more efficiently than retrograde ones, whereas the difference in angular-momentum loss between the two cases is much less prominent. For ex-

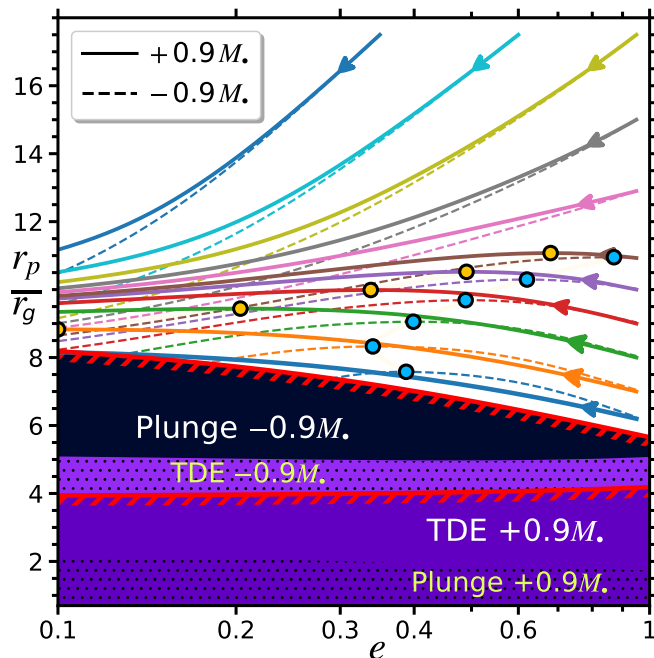


FIG. 6. Evolution in the (r_p, e) parameter space for WD-IMBH binaries whose orbital dynamics are driven by GW emission and TD. Solid curves correspond to a spin of $a = 0.9M_\bullet$ and the dashed one to $-0.9M_\bullet$. The yellow and blue dots on these curves mark where r_p reaches maximum, indicating equal contribution of TD and GW in determining the orbital dynamics. Shaded regions show where TDEs and plunges will happen (see Section II B for details). The other parameters are the same as in FIG. 4.

ample, at a pericenter distance of $r_p \simeq 10r_g$ in FIG. 5, the ratio of energy loss $\dot{E}_{\text{GR}}/\dot{E}_{\text{New}}$ is ~ 0.7 for prograde orbits, but decreases to ~ 0.4 for retrograde ones. Meanwhile, the corresponding ratio for angular-momentum loss, $\dot{L}_{\text{GR}}/\dot{L}_{\text{New}}$ remains nearly constant at ~ 0.7 – 0.8 for both cases. This different dependence of energy and angular-momentum losses on IMBH spin leads to a faster circularization (leftward drift in FIG. 6) of prograde orbits.

Noticeably, in a small region of parameter space with $6r_g \lesssim r_p \lesssim 10r_g$ and $e \gtrsim 0.4$, the prograde and retrograde orbits behave differently from the general trend discussed above. In this regime, TD dominates over GW backreaction, and, as shown in FIG. 5, retrograde orbits dissipate more orbital energy than prograde ones. As a result, the pericenters of retrograde orbits increase more significantly during circularization, for the same reason discussed in Sec. IV A.

V. GRAVITATIONAL WAVE SIGNATURES

To obtain the GW signals, we first compute the inspiral of a WD-IMBH binary by evolving the constants of motion using the fluxes. The GW flux is calculated us-

ing the Teukolsky equation [104–106], and the TD flux is computed using the method described in Sec. III C. From these fluxes, we get a time evolution of quasi-Keplerian orbital parameters $[p(t), e(t)]$. Since we confine our study to equatorial orbits, $x_I = \cos \iota = 1$, where ι is the orbital inclination from the equatorial plane.

The GW waveform is computed in the frequency domain, in which the $+$ - and \times -polarizations of the GW strain can be written as

$$h_+ + ih_\times = \sum_{\ell mnk} \mathcal{A}_{\ell nkm} {}^s S_{\ell m}(\theta, \hat{\omega}_{nkm}) e^{i(m\varphi - \hat{\omega}_{nkm}t)} \quad (19)$$

[107, 108], where $\mathcal{A}_{\ell nkm}$ is the GW amplitude, ${}^s S_{\ell m}$ is the spin-weighted spheroidal harmonics (for gravitational perturbations we consider $s = -2$), and $\hat{\omega}_{nkm} = n\hat{\omega}_r + k\hat{\omega}_\theta + m\hat{\omega}_\varphi$ are the fundamental frequencies. In particular, $\mathcal{A}_{\ell nkm}$ and $\hat{\omega}_{nkm}$ are functions of p and e , and since these evolve with time, we would in principle need to compute $\mathcal{A}_{\ell nkm}$ and $\hat{\omega}_{nkm}$ for every time-step in the orbital evolution. However, in practice, performing such a real-time calculation of the orbital evolution is far too costly, so we resort to interpolation schemes similar to those in `FastEMRIWaveforms` [98–101]. We first compute a grid of values for $\mathcal{A}_{\ell nkm}$ and $\hat{\omega}_{nkm}$ varying p and e using the `pybhpt` software package [102, 103]. Then, we create an interpolant for each $\mathcal{A}_{\ell nkm}$ and $\hat{\omega}_{nkm}$ using Chebyshev polynomials. Finally, we use the interpolant to extract $\mathcal{A}_{\ell nkm}$ and $\hat{\omega}_{nkm}$ and, according to Equation (19), sum up each mode contribution up to a tolerance of $\epsilon = 10^{-8}$ to derive h_+ and h_\times .

In FIG. 7, we compare the GW signal of a WD-IMBH binary driven by GW radiation and TD versus the signal of a binary driven purely by GW radiation. The orbital parameters are chosen such that the WD is far from the TDE radius, so that GW radiation predominates. The corresponding GW radiation timescale is about 10^3 yrs. Despite the secondary role of TD in the orbital dynamics, the subtle orbital change accumulates coherently over time, so that in about two years the differences in GW amplitude and phase are clearly discernible in the time-domain waveform (compare top and middle panels).

In the bottom panel, we compare the characteristic strains and find that the higher harmonics of the GW signals are in the detection band of LISA and TianQin. The SNRs for LISA and TianQin are $\rho_{\text{LISA}} = 16$ and $\rho_{\text{TQ}} = 4.8$, and the matches between the waveforms with and without TD are $\mathcal{M}_{\text{LISA}} = 0.45$ and $\mathcal{M}_{\text{TQ}} = 0.53$, respectively. Here, \mathcal{M} is defined by

$$\mathcal{M}(h, \tilde{h}) = \frac{\langle \tilde{h} | \tilde{h} \rangle}{\sqrt{\langle \tilde{h} | \tilde{h} \rangle \langle \tilde{h} | \tilde{h} \rangle}}, \quad (20)$$

where $\langle \tilde{h} | \tilde{h} \rangle$ denotes the noise-weighted inner product of the Fourier transformed waveforms \tilde{h} and \tilde{h} [116–119]. These small values of \mathcal{M} indicate that LISA can detect such a binary and discern the TD effects, and hence distinguish the WD from other compact objects, since the

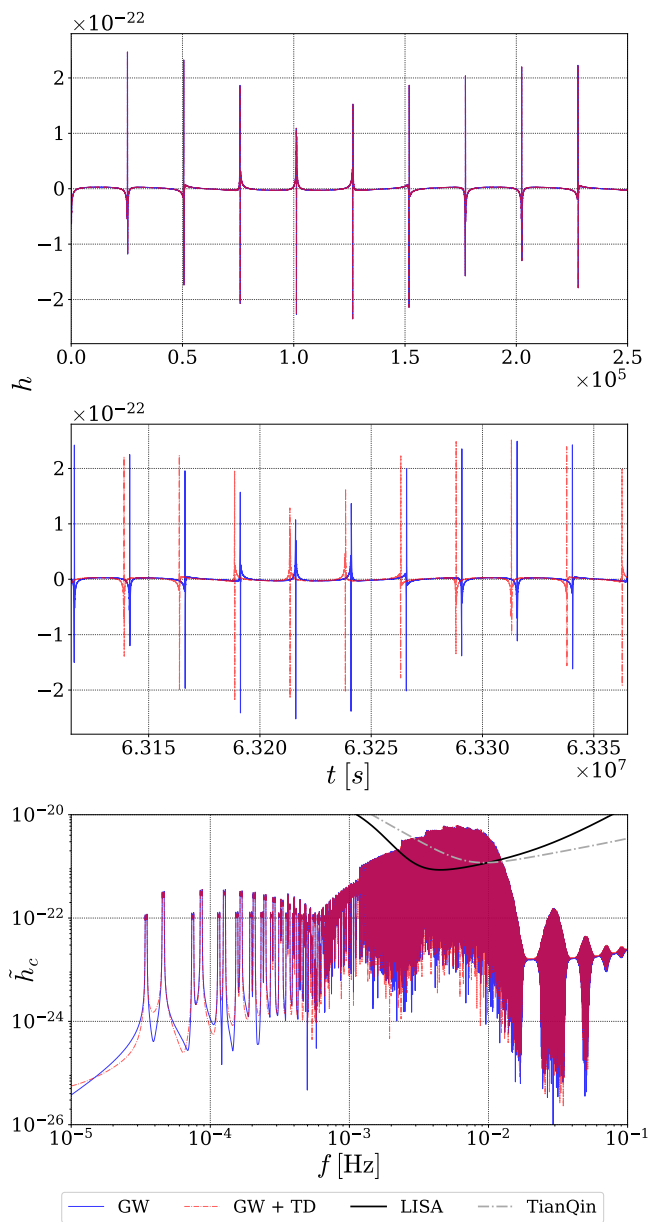


FIG. 7. Time-domain waveforms at early (top panel) and late (middle panel) times, and the frequency-domain characteristic strains (bottom panel) for binaries driven purely by GW radiation (blue solid curve) versus those binaries with TD and GW radiation (red dot-dashed curve). Noise curves of LISA (black line) [109–113] and TianQin (gray dot-dashed line) [114, 115] are also shown in the bottom panel. The initial orbital parameters are $(M_*, M_\bullet, a, r_p, e, x_I) = (0.6M_\odot, 10^5 M_\odot, 0.9M_\bullet, 20r_g, 0.95, 1)$, and the luminosity distance is $d_L = 50$ Mpc. The waveforms are computed over the projected 4-year observation time of LISA.

threshold for detection is normally $\rho > 10$ and the criterion of distinguishing two different waveforms is roughly $1 - \mathcal{M} > 1/(2\rho^2)$ [120]. However, despite the lower SNR value, TianQin could be useful for detecting the TD effects in less distant WD-IMBH binaries with smaller peri-

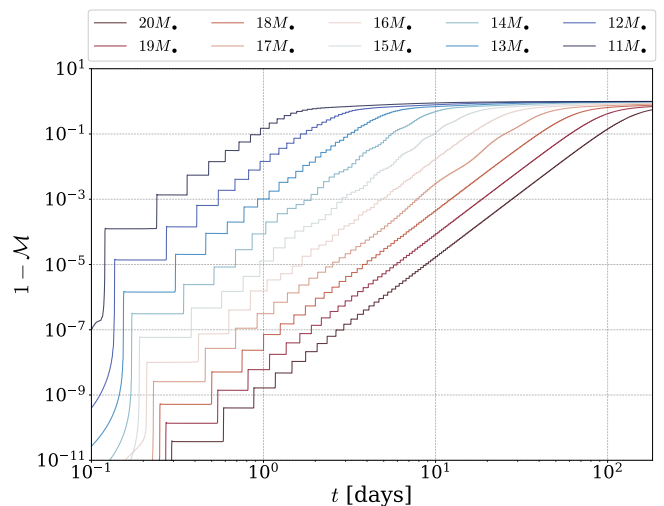


FIG. 8. Time evolution of the mismatch between the waveforms with and without TD effects over an observation period of six months. Different lines correspond to different pericenter distances for the WD-IMBH binaries. Here we use the noise curve for LISA [109–113], and the other initial orbital parameters are the same as in FIG. 7.

center distances [121].

We further verify this assertion by plotting the mismatch as a function of time in FIG. 8, and find that the mismatch can reach unity within a six-month observation period. Observe that as r_p decreases, the mismatch grows more rapidly in time. This is physically consistent since the TD effects become dominant for pericenter distances close to the IMBH.

VI. DISCUSSION AND CONCLUSION

Motivated by the prospect of observing a WD-IMBH system in both EM and GW bands, we studied in this work the dynamical evolution of such a system and its GW signals, with a focus on developing a relativistic model for the response of the WD to the tidal force of the IMBH. We first examined the physical scales and timescales of the system (Sec. II), finding that strong tidal interaction occurs in the strong-gravity regime when the IMBH mass exceeds $10^5 M_\odot$ (FIG. 1). Therefore, relativistic corrections are necessary in modeling the tidal interactions in these systems. We also found that including the spin of the IMBH could result in a plunge of the WD into the black hole prior to complete tidal disruption (FIG. 1), especially for retrograde orbit. This result suggests that EM counterparts are more likely to be produced by those WDs on prograde orbits, which puts strong constraints on the formation channels of potential multi-messenger sources.

Before the plunge or full tidal disruption, the WD interacts with the IMBH secularly. We have developed a

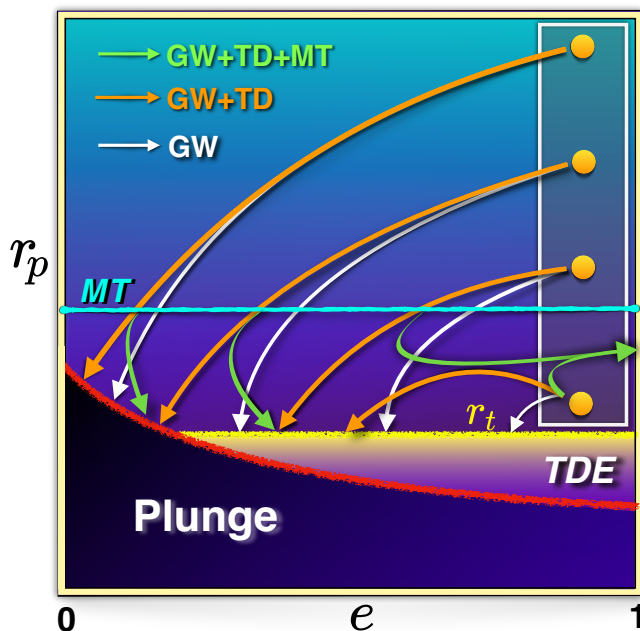


FIG. 9. Schematic illustration of WD orbital evolution in the (r_p, e) parameter space. Colored trajectories show evolution driven by GW emission alone or by GW combined with TD and MT. In addition, the cyan, yellow, and red solid lines indicate the onset of MT, the TDE boundary, and the direct-plunge boundary, respectively.

fully relativistic model to calculate the tidal force imposed on the WD, and derive the energy and angular-momentum loss from the binary orbit caused by the forced g -mode oscillation of the WD (Sec. III). Our main finding is that TD can be weaker in our relativistic model than in the previous Newtonian calculations (FIG. 5), despite the fact that the tidal field can be stronger in our relativistic case. The cause of this suppression of TD can be attributed to the loss of temporal phase coherence in tidal forcing, which is incurred by the rotation of the FNCs (see Sec. III A).

Using the relativistic TD rate, we calculated the secular evolution of the WD-IMBH orbit, also taking into account the effect of GW radiation (FIGs. 4 and 6). We find that TD becomes dynamically important once the pericenter distance approaches $\simeq (2 - 3) r_t$, corresponding to $r_p \simeq 15 r_g$ in our fiducial model. Moreover, TD leads to more rapid damping of the orbital eccentricity, to the extent that the pericenter distance may even increase over time. Such an increase in r_p can have important implications for QPEs, as it reduces the cumulative TD rate and delays complete orbital circularization, thereby prolonging the quasi-periodic flaring phase. In addition to modifying the flare lifetime, the orbital period evolution may also be affected. Although TD alone cannot increase the orbital period under mass conservation, its coupling

with mass transfer may lead to orbital expansion, potentially accounting for the secular period growth reported in some QPE systems [122, 123].

The TD of orbital energy implies that a substantial amount of energy is deposited into the hydrogen envelope of the WD [54]. According to our model, the energy dissipation rate can reach $10^{32} - 10^{33} \text{ erg s}^{-1}$. If a significant fraction is used to heat the hydrogen envelope, the heating rate already exceeds the typical cooling luminosity of a WD (e.g., $\sim 10^{-3} L_\odot \sim 10^{30} \text{ erg s}^{-1}$ for a $0.6 M_\odot$ WD) by orders of magnitude. Therefore, the envelope cannot radiate the injected energy fast enough, and the temperature will increase. If the increased temperature triggers thermonuclear runaway at the base of the envelope, a nova-like flash would occur. Such a transient EM counterpart deserves future investigation.

Finally, we studied the cumulative effect of TD on the GW signal (Sec. V). We found that even small TD-induced orbital changes, over many pericenter passages, accumulate and produce measurable phase shifts in GW data. As shown in FIG. 8, the mismatch can reach ~ 0.1 within months of observation, indicating that TD effects are, in principle, distinguishable in space-based GW data. This suggests that WD-IMBH binaries may be identified not only by their masses but also through tidal imprints in their waveforms, providing a novel probe of WD internal structure.

While the present work has focused on equatorial Kerr orbits and g -mode excitation, additional physical processes may further affect dissipation and introduce cycle-to-cycle variability. For example, f -mode excitation, WD spin, and generic orbital inclination are still missing in the current model. In addition, MT will occur when r_p approaches the tidal-disruption radius, and previous works have shown that it may increase eccentricity and, in rare cases, render the orbit unbound [51, 52]. FIG. 9 schematically illustrates the possible outcomes under different initial conditions and physical processes. The regime where these outcomes diverge the most corresponds to small pericenter distances, highlighting the importance of general relativistic corrections. Therefore, a fully relativistic treatment of the TD and MT processes in WD-IMBH systems is essential for making reliable predictions of their multi-messenger signals, and our work may have provided a useful first step.

VII. ACKNOWLEDGEMENTS

This work is supported by the National Key Research and Development Program of China (Grant No. 2021YFC2203002) and the National Natural Science Foundation of China (Grant No. 12473037). ATO acknowledges support by the National Science Foundation of China (No. W2533010). ATO and LL were supported by Beijing Natural Science Foundation (No. IS25014).

- [1] M. Volonteri, *Astron. Astrophys. Rev.* **18**, 279 (2010).
- [2] M. A. Latif and A. Ferrara, *Publications of the Astronomical Society of Australia* **33**, e051 (2016).
- [3] K. Inayoshi, E. Visbal, and Z. Haiman, *Annu. Rev. Astron. Astrophys.* **58**, 27 (2020).
- [4] J. Kormendy and L. C. Ho, *Annu. Rev. Astron. Astrophys.* **51**, 511 (2013).
- [5] J. Silk, *Astrophys. J. Lett.* **839**, L13 (2017).
- [6] J. E. Greene, J. Strader, and L. C. Ho, *Annual Review of Astron and Astrophysics* **58**, 257 (2020).
- [7] A. E. Reines and A. Comastri, *Publications of the Astron. Soc. of Australia* **33**, e054 (2016).
- [8] M. Mezcuca, *International Journal of Modern Physics D* **26**, 1730021 (2017).
- [9] R. Abbott, H. Abe, F. Acernese, K. Ackley, N. Adhikari, R. X. Adhikari, V. K. Adkins, V. B. Adya, C. Affeldt, D. Agarwal, *et al.* (LIGO Scientific Collaboration, Virgo Collaboration, and KAGRA Collaboration), *Phys. Rev. D* **106**, 102008 (2022).
- [10] T. L. S. Collaboration, the Virgo Collaboration, and the KAGRA Collaboration, *Open data from ligo, virgo, and kagra through the first part of the fourth observing run* (2025), [arXiv:2508.18079 \[gr-qc\]](https://arxiv.org/abs/2508.18079).
- [11] D. J. Reardon, A. Zic, R. M. Shannon, G. B. Hobbs, M. Bailes, V. Di Marco, A. Kapur, A. F. Rogers, E. Thrane, J. Askew, *et al.*, *The Astrophysical Journal Letters* **951**, L6 (2023).
- [12] H. Xu, S. Chen, Y. Guo, J. Jiang, B. Wang, J. Xu, Z. Xue, R. Nicolas Caballero, J. Yuan, Y. Xu, *et al.*, *Research in Astronomy and Astrophysics* **23**, 075024 (2023).
- [13] J. Antoniadis *et al.* (EPTA, InPTA), *Astron. Astrophys.* **678**, A49 (2023).
- [14] M. T. Miles, R. M. Shannon, D. J. Reardon, M. Bailes, D. J. Champion, M. Geyer, P. Gitika, K. Grunthal, M. J. Keith, M. Kramer, *et al.*, *Monthly Notices of the Royal Astronomical Society* **536**, 1489–1500 (2024).
- [15] G. Agazie, A. Anumrapudi, A. M. Archibald, Z. Arzoumanian, J. G. Baier, P. T. Baker, B. Bécsy, L. Blecha, A. Brazier, P. R. Brook, *et al.* (NANOGrav Collaboration), *Phys. Rev. D* **111**, 042011 (2025).
- [16] D. Hils and P. L. Bender, *Astrophys. J. Lett.* **445**, L7 (1995).
- [17] H. Baumgardt, J. Makino, and T. Ebisuzaki, *The Astrophysical Journal* **613**, 1143–1156 (2004).
- [18] L. Blecha, N. Ivanova, V. Kalogera, K. Belczynski, J. Fregeau, and F. Rasio, *The Astrophysical Journal* **642**, 427–437 (2006).
- [19] M. A. Gürkan, J. M. Fregeau, and F. A. Rasio, *The Astrophysical Journal* **640**, L39–L42 (2006).
- [20] P. Amaro-Seoane and M. Freitag, *The Astrophysical Journal* **653**, L53–L56 (2006).
- [21] J. Luo, L.-S. Chen, H.-Z. Duan, Y.-G. Gong, S. Hu, J. Ji, Q. Liu, J. Mei, V. Milyukov, M. Sazhin, *et al.*, *Classical and Quantum Gravity* **33**, 035010 (2016).
- [22] Z. Luo, Y. Wang, Y. Wu, W. Hu, and G. Jin, *Progress of Theoretical and Experimental Physics* **2021**, 05A108 (2021).
- [23] P. Amaro-Seoane, J. Andrews, M. Arca Sedda, A. Askar, Q. Baghi, R. Balasov, I. Bartos, S. S. Bavera, J. Bellovary, *et al.*, *Living Reviews in Relativity* **26**, 10.1007/s41114-022-00041-y (2023).
- [24] P. Ajith, P. A. Seoane, M. A. Sedda, R. Arcodia, F. Badaracco, B. Banerjee, E. Belgacem, G. Benetti, S. Benetti, A. Bobrick, *et al.*, *Journal of Cosmology and Astroparticle Physics* **2025** (01), 108.
- [25] P. B. Ivanov and J. C. B. Papaloizou, *Astron. Astrophys.* **476**, 121 (2007).
- [26] K. Menou, Z. Haiman, and B. Kocsis, *New Astronomy Reviews* **51**, 884 (2008), jean-Pierre Lasota, X-ray Binaries, Accretion Disks and Compact Stars.
- [27] A. Sesana, A. Vecchio, M. Eracleous, and S. Sigurdsson, *Mon. Not. R. Astron. Soc.* **391**, 718 (2008).
- [28] I. Zalamea, K. Menou, and A. M. Beloborodov, *Monthly Notices of the Royal Astronomical Society: Letters* **409**, L25 (2010).
- [29] J.-P. Luminet and B. Pichon, *Astron. Astrophys.* **209**, 103 (1989).
- [30] S. Rosswog, E. Ramirez-Ruiz, and W. R. Hix, *Astrophys. J.* **695**, 404 (2009).
- [31] M. MacLeod, J. Goldstein, E. Ramirez-Ruiz, J. Guillochon, and J. Samsing, *The Astrophysical Journal* **794**, 9 (2014).
- [32] J.-H. Chen, R.-F. Shen, and S.-F. Liu, *The Astrophysical Journal* **947**, 32 (2023).
- [33] D. Hils and P. L. Bender, *Astrophys. J. Lett.* **445**, L7 (1995).
- [34] B. Kocsis, N. Yunes, and A. Loeb, *Phys. Rev. D* **84**, 024032 (2011).
- [35] H. Pfister, M. Toscani, T. H. T. Wong, J. L. Dai, G. Lodato, and E. M. Rossi, *Mon. Not. R. Astron. Soc.* **510**, 2025 (2022).
- [36] S. Kejriwal, V. Witzany, M. Zajaček, D. R. Pasham, and A. J. K. Chua, *Mon. Not. R. Astron. Soc.* **532**, 2143 (2024).
- [37] L. Dai, S. V. Fuerst, and R. Blandford, *Mon. Not. Roy. Astron. Soc.* **402**, 1614 (2010).
- [38] L. Dai and R. D. Blandford, *Mon. Not. Roy. Astron. Soc.* **434**, 2948 (2013).
- [39] J. Xian, F. Zhang, L. Dou, J. He, and X. Shu, *The Astrophysical Journal Letters* **921**, L32 (2021).
- [40] M. Wang, J. Yin, Y. Ma, and Q. Wu, *The Astrophysical Journal* **933**, 225 (2022).
- [41] A. King, *Mon. Not. R. Astron. Soc.* **515**, 4344 (2022).
- [42] X. Chen, Y. Qiu, S. Li, and F. K. Liu, *The Astrophysical Journal* **930**, 122 (2022).
- [43] Zhao, Z. Y., Wang, Y. Y., Zou, Y. C., Wang, F. Y., and Dai, Z. G., *Astron. Astrophys.* **661**, A55 (2022).
- [44] T. Suzuguchi, H. Omiya, and H. Takeda, *Possibility of multi-messenger observations of quasi-periodic eruptions with x-rays and gravitational waves* (2025), [arXiv:2505.10488 \[astro-ph.HE\]](https://arxiv.org/abs/2505.10488).
- [45] L. Lui, A. Torres-Orjuela, R. K. Chowdhury, and L. Dai, *Gravitational wave signatures of quasi-periodic eruptions: LISA detection prospects for rx j1301.9+2747* (2025), [arXiv:2508.07961 \[astro-ph.HE\]](https://arxiv.org/abs/2508.07961).
- [46] E. Neights, O. J. Roberts, E. Burns, P. Veres, E. Bissaldi, and Fermi-GBM Team, *GRB Coordinates Network* **40931**, 1 (2025).
- [47] D. Li, W. Zhang, J. Yang, J.-H. Chen, W. Yuan, H. Cheng, F. Xu, X. Shu, R.-F. Shen, N. Jiang, *et al.*, *arXiv e-prints*, [arXiv:2509.25877](https://arxiv.org/abs/2509.25877) (2025).

- [48] A. J. Levan, A. Martin-Carrillo, T. Laskar, R. A. J. Eyles-Ferris, A. Sneppen, M. E. Ravasio, J. C. Rastinejad, J. S. Bright, F. Carotenuto, A. A. Chrimes, *et al.*, *Astrophys. J. Lett.* **990**, L28 (2025).
- [49] R. A. J. Eyles-Ferris, A. King, R. L. C. Starling, P. G. Jonker, A. J. Levan, A. Martin-Carrillo, T. Laskar, J. C. Rastinejad, N. Sarin, N. R. Tanvir, *et al.*, *Monthly Notices of the Royal Astronomical Society*, stag005 (2026).
- [50] A. King, *Monthly Notices of the Royal Astronomical Society: Letters* **493**, L120 (2020).
- [51] D. Wang, *Astron. Astrophys.* **687**, A295 (2024).
- [52] Y. Yang, J. Yang, X. Chen, and Z.-H. Zhang, *Mon. Not. R. Astron. Soc.* **543**, 3503 (2025).
- [53] D. Lai, *The Astrophysical Journal* **490**, 847 (1997).
- [54] M. Vick, D. Lai, and J. Fuller, *Monthly Notices of the Royal Astronomical Society* **468**, 2296 (2017).
- [55] S. Y. Lau and H. Yu, *Phys. Rev. D* **112**, 103024 (2025).
- [56] P. Amaro-Seoane, J. R. Gair, M. Freitag, M. C. Miller, I. Mandel, C. J. Cutler, and S. Babak, *Classical and Quantum Gravity* **24**, R113 (2007).
- [57] J. a. Marck, *Proceedings of the Royal Society of London. A. Mathematical and Physical Sciences* **385**, 431 (1983).
- [58] M. Ishii, M. Shibata, and Y. Mino, *Phys. Rev. D* **71**, 044017 (2005).
- [59] R. M. Cheng and C. R. Evans, *Phys. Rev. D* **87**, 104010 (2013).
- [60] G. Miniutti, R. D. Saxton, M. Giustini, K. D. Alexander, R. P. Fender, I. Heywood, I. Monageng, M. Coriat, A. K. Tzioumis, A. M. Read, *et al.*, *Nature (London)* **573**, 381 (2019).
- [61] M. Giustini, G. Miniutti, and R. D. Saxton, *Astron. Astrophys.* **636**, L2 (2020).
- [62] R. Arcodia *et al.*, *Nature* **592**, 704 (2021).
- [63] J. Chakraborty, E. Kara, M. Masterson, M. Giustini, G. Miniutti, and R. Saxton, *Astrophys. J. Lett.* **921**, L40 (2021).
- [64] O. G. Benvenuto and L. G. Althaus, *Mon. Not. R. Astron. Soc.* **303**, 30 (1999).
- [65] L. S. Finn and K. S. Thorne, *Phys. Rev. D* **62**, 124021 (2000).
- [66] L. Barack and C. Cutler, *Phys. Rev. D* **70**, 122002 (2004).
- [67] W. H. Press and S. A. Teukolsky, *The Astrophysical Journal* **213**, 183 (1977).
- [68] J. Fuller and D. Lai, *Monthly Notices of the Royal Astronomical Society* **421**, 426 (2012).
- [69] P. B. Ivanov and J. C. B. Papaloizou, *Monthly Notices of the Royal Astronomical Society* **347**, 437 (2004).
- [70] C. M. Will, in *Gravity: Where Do We Stand?*, edited by R. Peron, M. Colpi, V. Gorini, and U. Moschella (2016) p. 9.
- [71] J. G. Hills, *Nature (London)* **254**, 295 (1975).
- [72] M. J. Rees, *Nature (London)* **333**, 523 (1988).
- [73] J. M. Bardeen, W. H. Press, and S. A. Teukolsky, *Astrophys. J.* **178**, 347 (1972).
- [74] K. Glampedakis and D. Kennefick, *Phys. Rev. D* **66**, 044002 (2002).
- [75] J. Levin and G. Perez-Giz, *Phys. Rev. D* **79**, 124013 (2009).
- [76] C. W. Misner, K. S. Thorne, J. A. Wheeler, and D. I. Kaiser, *Gravitation* (2018).
- [77] L. C. Stein and N. Warburton, *Phys. Rev. D* **101**, 064007 (2020).
- [78] M. Kesden, *Phys. Rev. D* **85**, 024037 (2012).
- [79] E. M. Rossi, N. C. Stone, J. A. P. Law-Smith, M. Macleod, G. Lodato, J. L. Dai, and I. Mandel, *Space Science Reviews* **217**, 40 (2021).
- [80] W. Xin and A. Mummery, *The relativistic tidal tensor: general solutions for stationary axisymmetric spacetimes and the hills mass of naked singularities* (2025), arXiv:2511.21499 [gr-qc].
- [81] P. C. Peters and J. Mathews, *Phys. Rev.* **131**, 435 (1963).
- [82] P. C. Peters, *Phys. Rev.* **136**, B1224 (1964).
- [83] H. Yu, N. N. Weinberg, and J. Fuller, *Monthly Notices of the Royal Astronomical Society* **496**, 5482 (2020).
- [84] F. K. Manasse and C. W. Misner, *Journal of Mathematical Physics* **4**, 735 (1963).
- [85] R. P. Kerr, *Phys. Rev. Lett.* **11**, 237 (1963).
- [86] B. Carter, *Phys. Rev.* **174**, 1559 (1968).
- [87] L. V. Drummond and S. A. Hughes, *Phys. Rev. D* **105**, 124040 (2022).
- [88] L. V. Drummond and S. A. Hughes, *Phys. Rev. D* **105**, 124041 (2022).
- [89] V. Skoupý and V. c. v. Witzany, *Phys. Rev. Lett.* **134**, 171401 (2025).
- [90] P. Brassard, G. Fontaine, F. Wesemael, S. D. Kawaler, and M. Tassoul, *Astrophys. J.* **367**, 601 (1991).
- [91] J. Fuller and D. Lai, *Monthly Notices of the Royal Astronomical Society* **430**, 274 (2013).
- [92] R. G. Barrera, G. A. Estevez, and J. Giraldo, *European Journal of Physics* **6**, 287 (1985).
- [93] K. S. Thorne, *Reviews of Modern Physics* **52**, 299 (1980).
- [94] Y. Mino, *Phys. Rev. D* **67**, 084027 (2003).
- [95] R. Fujita and W. Hikida, *Classical and Quantum Gravity* **26**, 135002 (2009).
- [96] S. Park and Z. Nasipak, *Journal of Open Source Software* **9**, 6587 (2024).
- [97] C. Dyson and M. van de Meent, *Class. Quant. Grav.* **40**, 195026 (2023).
- [98] A. J. K. Chua, C. R. Galley, and M. Vallisneri, *Phys. Rev. Lett.* **122**, 211101 (2019).
- [99] A. J. K. Chua, M. L. Katz, N. Warburton, and S. A. Hughes, *Phys. Rev. Lett.* **126**, 051102 (2021).
- [100] M. L. Katz, A. J. K. Chua, L. Speri, N. Warburton, and S. A. Hughes, *Phys. Rev. D* **104**, 064047 (2021).
- [101] C. E. A. Chapman-Bird, L. Speri, Z. Nasipak, O. Burke, M. L. Katz, A. Santini, S. Kejriwal, P. Lynch, J. Mathews, H. Khalvati, *et al.*, *Phys. Rev. D* **112**, 104023 (2025).
- [102] Z. Nasipak, *Phys. Rev. D* **106**, 064042 (2022).
- [103] Z. Nasipak, *Phys. Rev. D* **109**, 044020 (2024).
- [104] S. A. Teukolsky, *Phys. Rev. Lett.* **29**, 1114 (1972).
- [105] S. A. Teukolsky, *Astrophys. J.* **185**, 635 (1973).
- [106] S. A. Teukolsky and W. H. Press, *Astrophys. J.* **193**, 443 (1974).
- [107] S. Drasco and S. A. Hughes, *Phys. Rev. D* **69**, 044015 (2004).
- [108] S. Drasco and S. A. Hughes, *Phys. Rev. D* **73**, 024027 (2006).
- [109] N. J. Cornish and L. J. Rubbo, *Phys. Rev. D* **67**, 022001 (2003).
- [110] S. Babak, H. Fang, J. R. Gair, K. Glampedakis, and S. A. Hughes, *Phys. Rev. D* **75**, 024005 (2007).
- [111] A. Klein, E. Barausse, A. Sesana, A. Petiteau, E. Berti, S. Babak, J. Gair, S. Aoudia, I. Hinder, F. Ohme, and B. Wardell, *Phys. Rev. D* **93**, 024003 (2016).

- [112] P. Amaro-Seoane *et al.*, [Living Reviews in Relativity](#) **26**, 2 (2023).
- [113] M. Colpi *et al.*, [arXiv e-prints](#), arXiv:2402.07571 (2024).
- [114] J. Mei *et al.*, [Progress of Theoretical and Experimental Physics](#) **2021**, 05A107 (2021).
- [115] E.-K. Li *et al.*, [Reports on Progress in Physics](#) **88**, 056901 (2025).
- [116] B. J. Owen, [Phys. Rev. D](#) **53**, 6749 (1996).
- [117] S. D. Mohanty, [Phys. Rev. D](#) **57**, 630 (1998).
- [118] M. Pürrer and C.-J. Haster, [Phys. Rev. Res.](#) **2**, 023151 (2020).
- [119] E. Pizzati, S. Sachdev, A. Gupta, and B. S. Sathyaprakash, [Phys. Rev. D](#) **105**, 104016 (2022).
- [120] L. Lindblom, B. J. Owen, and D. A. Brown, [Phys. Rev. D](#) **78**, 124020 (2008).
- [121] A. Torres-Orjuela, S.-J. Huang, Z.-C. Liang, S. Liu, H.-T. Wang, C.-Q. Ye, Y.-M. Hu, and J. Mei, [Science China Physics, Mechanics, and Astronomy](#) **67**, 259511 (2024).
- [122] M. Masterson, E. Kara, C. Panagiotou, W. N. Alston, J. Chakraborty, K. Burdge, C. Ricci, S. Laha, I. Arcavi, R. Arcodia, *et al.*, [Nature](#) **638**, 370 (2025).
- [123] J. Chakraborty, S. A. Rappaport, R. Arcodia, I. Linnal, G. Miniutti, K. B. Burdge, J. Cuadra, M. Giustini, L. Hernández-García, E. Kara, *et al.*, [A positive period derivative in the quasi-periodic eruptions of ZTF19acnsky](#) (2026), arXiv:2602.16776 [astro-ph.HE].